Electro-Opto-Mechanical Effects in Swollen Nematic Elastomers

Kenji Urayama

Abstract Nematic elastomers swollen by low molecular weight nematogens (nematic gels) exhibit fast response to electric fields with a large change in optical birefringence together with macroscopic deformation. This electro-opto-mechanical (EOM) effect is a direct consequence of the deformation coupled to electrically driven director rotation in nematic gels under a mechanically unconstrained geometry. This article describes the static and dynamic features of the EOM effects of nematic gels. We will discuss recent investigations into the influences of field strength, frequency, and external mechanical constraints on the EOM effects. The relation between director rotation and macroscopic deformation is elucidated on the basis of optical and mechanical data in a steady state. The dynamics of the EOM effects are also discussed, on the basis of optical and mechanical response times to field imposition and removal. We also introduce a simple model to capture the main features of the static and dynamic aspects of the EOM effects.

Contents

K. Urayama
Department of Materials Chemistry, Kyoto University, Nishikyo-ku, Kyoto 615-8510, Japan
e-mail: urayama@rheogate.polym.kyoto-u.ac.jp

1   Introduction

Liquid crystal elastomers (LCEs) are, as the name implies, hybrid materials composed of liquid crystals (LCs) and elastomers. A marked characteristic of LCEs is a strong coupling between the macroscopic shape and the molecular orientation of the constituent mesogens. This strong coupling results in the unique stimulus-responsive properties of LCEs [1–4]. When an external field alters the degree or direction of mesogen orientation in LCEs, a corresponding change in the macroscopic shape occurs simultaneously. As a familiar example, a temperature variation causes finite uniaxial deformation of nematic elastomers as a result of a change in the orientational order of the mesogens, the details of which are described by Kramer et al. [5].

Electric field is also expected as an effective external field to drive finite and fast deformation in LCEs, because, as is well known for low molecular mass LCs (LMM-LCs), an electric field is capable of inducing fast rotation of the director toward the field direction [6]. This electrically driven director rotation results in a large and fast change in optical birefringence that is called the electro-optical (EO) effect. The EO effect is a key principle of LC displays. Electrically induced deformation of LCEs is also attractive when they are used for soft actuators: a fast actuation is expected, and electric field is an easily controlled external variable. However, in general, it is difficult for LCEs in the neat state to exhibit finite deformation in response to the modest electric fields accessible in laboratories. Some chiral smectic elastomers in the neat state show finite deformation stemming from electroclinic effects [7, 8], but that is beyond the scope of this article; we focus on deformation by director rotation.

Early work by Zentel [9] and several other researchers [10–14] observed the electro-mechanical (EM) effect, i.e., finite distortions under modest electric fields, for the LCEs that were swollen by LMM-LCs. Swelling by miscible LMM-LCs considerably softens LCEs without losing their liquid crystallinity. This softening significantly reduces the field strength required for actuation. However, the simultaneous mesogen reorientation (resulting in the EO effect) was too small to detect or not characterized in most of these studies.

Other groups [15, 16] studied the EO effect in monodomain nematic gels that were directly prepared in EO cells in the presence of a large amount of LMM-LC, but none of these studies clearly observed finite macroscopic deformation. The gel specimens

in these studies were effectively sandwiched between the two rigid electrodes, and this constrained geometry prevented strain in the field direction. A theoretical study [17] suggests that such a constraint significantly enhances the elastic barrier, and thus the field strength required for finite distortion becomes very high.

The strong coupling of director and macroscopic deformation in LCEs implies that the response to electric fields appears as EM effects accompanied by EO effects. This electro-opto-mechanical (EOM) effect was demonstrated using a monodomain nematic elastomer swollen by LMM-LC that was placed in an unconstrained geometry where the specimen had no mechanical constraints from electrodes [18, 19]. The combination of the monodomain sample with the unconstrained geometry facilitates director rotation and the resultant deformation under electric fields. In addition, the field-driven director configuration of unconstrained nematic elastomers is considerably different from that in the conventional Fredericks effects of nematic liquids. Figure 1 shows the schematics of the field-driven director configurations of nematic liquids and an unconstrained nematic elastomer slab floating in fluid between rigid electrodes. They both initially have a uniform planar configuration before the field imposition. In the case of nematic liquids (Fig. 1a), the directors at the surfaces are anchored, and the rotation angle of the director has a finite distribution, with the maximum at the middle layer of the cell. The recovery to the initial planar configuration in response to field-off originates from the Frank elasticity. In contrast, the director of unconstrained nematic elastomers (Fig. 1b) is capable of uniform rotation under electric fields. The Frank elasticity plays no role in the recovery to the initial configuration.

The EOM effect also provides an important basis for elucidating the correlation between the director rotation and macroscopic deformation. Experimentally, it has often been investigated by mechanically stretching the monodomain nematic elastomers in the direction normal to the initial director [20–25]. However, the mechanical constraint by clamping at the ends significantly affects the director rotation, and the resultant director reorientation often becomes inhomogeneous [26–28]. In contrast, the EOM effect in Fig. 1b enables us to observe unambiguously the characteristic
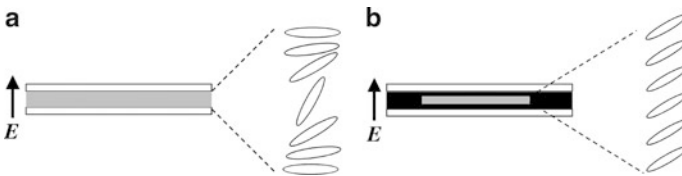

Fig. 1 Field-driven director configurations in (**a**) a nematic liquid (conventional Fredericks effect) and (**b**) a nematic elastomer slab floating in liquid between rigid electrodes. They initially have a uniform planar orientation before imposing field E in the direction shown by the *arrow*. In (**a**), the director at the surfaces are anchored, and the rotation angle of director has a finite distribution along the field axis, with the maximum at the middle layer of the cell. The recovery force for the director originates from the Frank elasticity. In (**b**), the director is capable of uniform rotation under electric fields, and the Frank elasticity plays no role in the recovery force

deformation mode driven by director rotation. Furthermore, the dynamic aspect of this phenomenon (i.e., the rate of response to the imposition and removal of electric fields) is an interesting issue, especially in view of the comparison with the dynamics of the EO effect in LMM-LCs. The dynamic properties are also important for exploring the possibility of this effect in novel soft actuators. A primary goal of this article is to review various aspects of the EOM effects that have been elucidated by recent studies.

In Sect. 2, we introduce the details of the materials and the experimental setup. Static features such as the voltage dependencies of optical birefringence and strain are described in Sect. 3. Polarized Fourier transform infrared spectroscopy (FTIR) studies to characterize the electrically driven mesogen realignment are also discussed in Sect. 3. Dynamic features of the optical and mechanical responses are described in Sect. 4. A simple model to capture the main characteristics of EOM effects is introduced in Sect. 5. Conclusions and directions for future research are given in Sect. 6.

2 Materials and Observation Geometry

2.1 Materials

Most of the investigations introduced in this article employed a side-chain-type nematic elastomer that has the polyacrylate backbone with cyanobiphenyl side group. This nematic elastomer was obtained by the photopolymerization of the monoacrylate mesogenic monomer (A-6OCB; Fig. 2) and the cross-linker 1,6 hexanediol diacrylate (HDDA; Fig. 2) using a miscible nonreactive LMM-LC as a solvent [29]. The mixing of the nonreactive nematic solvent with A-6OCB (1:1 by molar ratio) was required to broaden the temperature range of the nematic state, since the nematic phase of pure A-6OCB exists in a limited temperature range because of the high crystallizability.

To obtain monodomain nematic elastomers with a global orientation, the photopolymerization was performed in a glass cell whose surfaces were coated with uniaxially rubbed polyimide layers. In this glass cell, the nematic mixture in the low-temperature nematic state was allowed to align globally in the rubbing direction. The photopolymerization was conducted at a temperature in the nematic state by
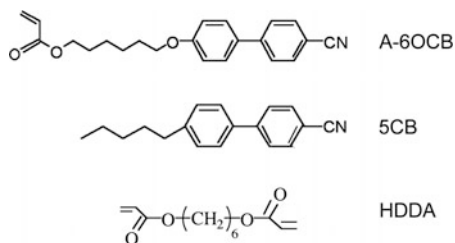

Fig. 2 Chemical structures of the mesogenic monoacrylate monomer (A-6OCB), cross-linker (HDDA), and the low molecular weight nematogen (5CB)

Table 1 Sample characteristics of monodomain nematic gels

| Nematic gel	Crosslinker concentration (c_x) (mol%)	Gel thickness (d_g^0) (μm)	Spacer thickness (d_p) (μm)	Cell gap (d_t) (μm)	Solvent content (vol%)
SNE-3	3	26	20	40	82
SNE-7	7	34	25	40	74
SNE-7D	7	43	40	50	78
SNE-10D	10	40	40	50	73
SNE-14	14	23	25	40	50

irradiating the cell using a wavelength of 526 nm. The cell gap was controlled using a spacer with a thickness of d_p ranging from 20 to 40 μm (Table 1). The cross-linker concentration (c_x) was varied from 3 to 14 mol%. The resulting gel films were carefully separated from the cell and immersed in dichloromethane to wash out the unreacted materials and nematic solvent. The swollen films were gradually deswollen by increasing the methanol content in the swelling solvent. The fully deswollen films were dried and thereafter allowed to swell in a cyanobiphenyl type LMM-LC, 4-*n*-pentyl-4′-cyanobiphenyl (5CB; Fig. 2) at 25°C until the swelling was equilibrated. The 5CB content in the swollen films increases with a decrease in c_x and ranged from 82 to 50 vol% (Table 1). In the fully swollen films, the LCE and 5CB are completely miscible and form a single nematic phase, which is confirmed by a single nematic-isotropic transition temperature [30]. It should be noted that both of the constituent nematogens, A-6OCB and 5CB, in the swollen elastomers are dielectrically positive, i.e., the molecular long axis of each nematogen tends to align parallel to the direction of electric fields.

2.2 Observation Geometry

As demonstrated later, unconstrained geometry is crucial for the observation of pronounced EOM effects. The swollen elastomer films were placed between two glass plates with optically transparent indium tin oxide (ITO) electrodes so that the films could have no mechanical constraints from the rigid electrodes, i.e., the cell gap was larger than the film thickness, as shown in Fig. 3. The cell was filled with a silicone oil, which was optically transparent and immiscible with the swollen elastomers, in order to observe the EO effect purely originating from the gels. The gel thickness (d_g^0) and cell gap (d_t) for each sample are listed in Table 1.

A square AC electric field was imposed normally on the initial director of the swollen elastomers. The frequency was 1 kHz unless specified otherwise. In the measurement of optical birefringence, the specimen was placed such that the initial director was at an angle of 45° relative to the crossed polarizers. The intensity of the transmitted light (I) was measured by a photodiode detector as a function of voltage amplitude (V_0). The effective birefringence in the *x–y* plane (Δn_{eff}) was evaluated

Fig. 3 Experimental setup for EOM effect and polarized FTIR measurements of nematic gels under electric fields. For the optical birefringence measurements, the initial director of the specimen has an angle of 45° relative to the crossed polarizers. For the polarized FTIR measurements, the optical axis of the polarizer is parallel or normal to the initial director for evaluating absorbances A_x or A_y, respectively, and no analyzer is used. l_x and l_y are the dimensions of the film in the x- and y-directions, respectively
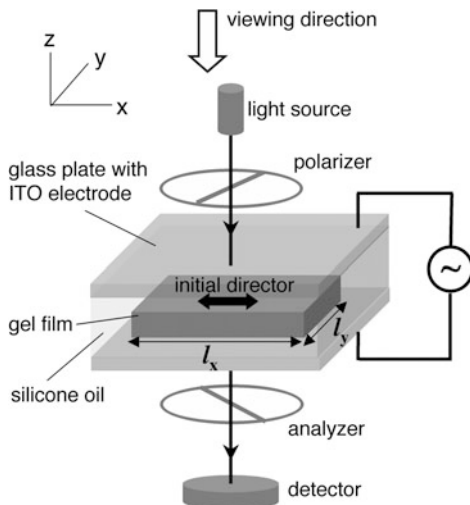
from the familiar relation $I/I_{max} = \sin^2(\pi d\Delta n_{eff}/\lambda)$ where λ is the wavelength of a He–Ne laser ($\lambda = 633$ nm). The change in film thickness (d) was less than 15% in the V_0 range examined, and thus the initial thickness was used for the sake of simplicity in the calculation of Δn_{eff} at each V_0.

The electrically induced strains in the x- and y-directions were measured using an optical microscope. The dimensional change in the z-direction (field axis) is not directly measurable, but can be straightforwardly estimated from the dimensional variations in the x- and y-directions because of the constant volume before and after deformation.

3 Static Aspects

3.1 Electro-Mechanical Effect

The most prominent feature of the electrical deformation of monodomain nematic gels in an unconstrained geometry is two-dimensional [18], as shown in Fig. 4a. The gel film contracts in the direction of the initial director (x-direction) and elongates in the field direction (z-direction) without an appreciable dimensional change in the y-direction normal to both the initial director and the field axis. The elongation in the z-direction is estimated from the dimensional changes in the x- and y-directions because the gel volume is constant during deformation. It should be noted that the y-direction without dimensional variation is identical to the axis of rotation of the director. An mpeg movie of this electrical deformation is available in the supporting information of [31].
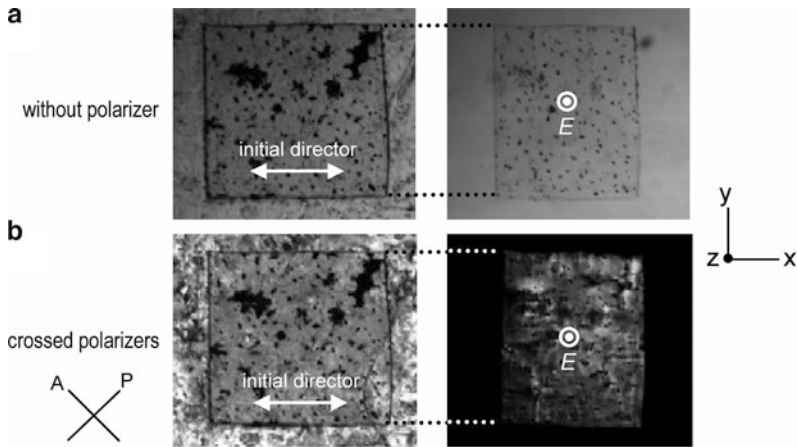
Fig. 4 Electro-opto-mechanical effect of a monodomain nematic gel observed (**a**) without polarizer and (**b**) with crossed polarizers. A 26-μm thick gel with $c_x = 4$ mol% is placed in a 40-μm thick EO cell filled with a nematic solvent (5CB). The 5CB content in the gel is 82 vol%. An AC field (E) with an amplitude of 750 V and a frequency of 1 kHz is imposed in the z-direction. The field induces a two-dimensional deformation, i.e., a shortening of ca. 20% in the x-direction, no dimensional change in the y-direction, and a lengthening of ca. 20% in the z-direction (due to volume conservation). The appearance of the gel (and surrounding 5CB) under cross-polarized conditions changes from bright to dark as a result of the almost full rotation of the director toward the field direction. A and P stand for the optical axes of analyzer and polarizer, respectively. An mpeg movie is available in the supporting information of [31]

Fig. 5 Strains γ_x (*closed symbols*) and γ_y (*open symbols*) as a function of voltage amplitude (V_0): SNE-3 (*squares*), SNE-7 (*circles*), SNE-14 (*triangles*). The *arrows* indicate the threshold voltage (V_{0c}) for the onset of deformation, and V_{0c} increases with c_x. The surrounding fluid in the EO cell (Fig. 3) is a silicone oil. From [19]
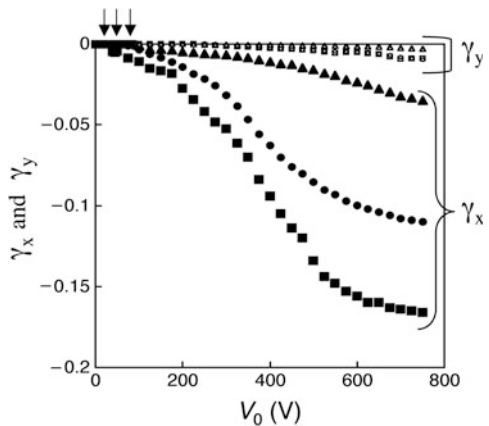
Figure 5 shows the strain in the x- and y-direction (γ_x and γ_y, respectively) as a function of voltage amplitude (V_0) for specimens with various cross-linker concentrations (c_x) [19]. The strain is defined by:

$$\gamma_i = \frac{l_i - l_{i0}}{l_{i0}} \tag{1}$$

where l_i ($i = x,y,z$) is the dimension in the i-direction and the subscript 0 denotes the undeformed state. As can be seen in Fig. 5, the contractive strain in the x-direction increases with V_0 above a threshold voltage amplitude (V_{0c}), and levels off at sufficiently high V_0. In contrast, γ_y remains almost zero even at high V_0. The two-dimensional deformation mode is independent of V_0 and c_x. A reduction in c_x increases the magnitude of the strain, and the maximum $|\gamma_x|$ reaches ca. 15% for $c_x = 3$ mol%. A decrease in c_x also reduces V_{0c}. A detailed discussion of V_{0c} will be given in Sect. 3.5.

Nematic gels with random polydomain textures under electric fields exhibit simple (three-dimensional) uniaxial deformation [13]. Figure 6 shows the electrical deformation of a cylindrical-shaped polydomain nematic gel in an unconstrained geometry. The chemical structures of the mesogen, the cross-linker, and the swelling solvent are identical to those of the monodomain samples in Figs. 4 and 5. The cross-linking reaction without taking mesogen alignment into account results in a nematic elastomer with a polydomain texture that possesses randomly oriented local directors without a global director. As shown in Fig. 6, the field-induced deformation is uniaxial elongation along the field axis: The dimension in the electric field increases, whereas the dimensions in the other two directions decrease equivalently. The directors have a random configuration in the initial state, and the electric field induces a rotation of the local directors toward the field direction.

The results shown in Figs. 4–6 were obtained for nematic gels with dielectrically positive mesogens whose molecular long axes are parallel to the dipole moment. The director of dielectrically positive nematogens aligns in the field direction. The electrical stretching of dielectrically positive nematic gels is parallel to the field direction, independently of the type of initial director configuration (monodomain or polydomain). Figure 7 shows the electrical deformation of a cylindrical-shaped polydomain nematic gel with negative dielectric anisotropy [13]. Both the mesogen and the swelling solvent in this gel, whose chemical structures are shown in Fig. 7a, are dielectrically negative (i.e., the long axes are normal to the dipole moment).
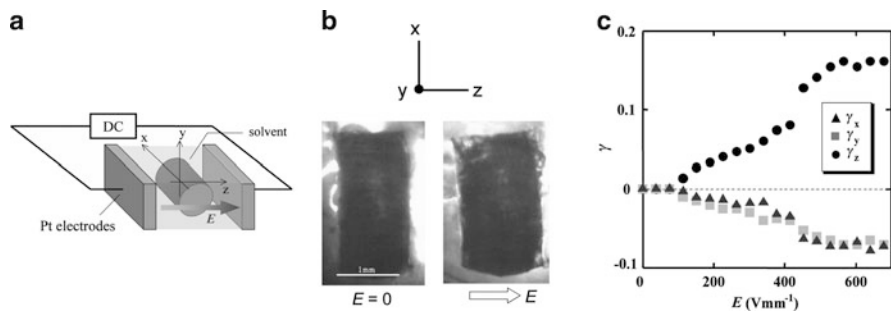

Fig. 6 Electro-mechanical effect of a cylindrical-shaped polydomain nematic gel with positive dielectric anisotropy. (**a**) Observation geometry. (**b**) Electrical deformation under a DC field of $E = 0.6$ MV/m. The specimen is elongated in the field direction and contracted in the other two directions. Observation under natural light. (**c**) Strains as a function of field strength. From [13]
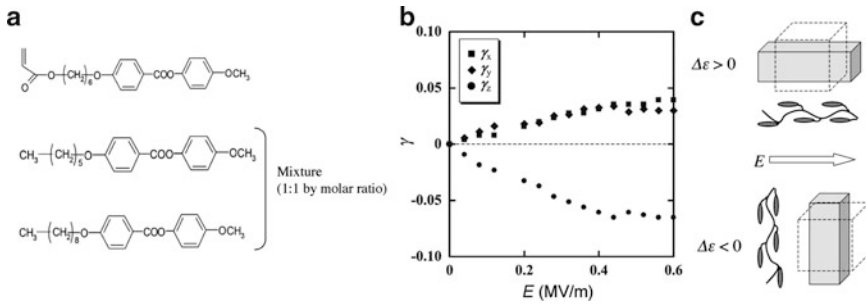
Fig. 7 Electro-mechanical effect of a cylindrical-shaped polydomain nematic gel with negative dielectric anisotropy. (**a**) Molecular structures of the constituent mesogen and swelling solvent in the gel. (**b**) Strains as a function of field strength. From [13]. (**c**) Schematics of electrical deformation of dielectrically positive ($\Delta\varepsilon > 0$) or negative ($\Delta\varepsilon < 0$) polydomain nematic gels. In the nematic gels in the present study (Fig. 2), the stretching direction of network backbone is parallel to the mesogen alignment [33, 34]

The dielectrically negative nematic gels are elongated in the direction normal to the field axis in accordance with the realignment direction of the local directors. These results indicate that the stretching direction in the electrical deformation of nematic gels is governed by the sign of the dielectric anisotropy, which is schematically shown in Fig. 7c. In general, the stretching direction of polymer backbone becomes either parallel or normal to the alignment direction of dangling mesogens, depending on the spacer length and the chemical structures of side-chain type LCEs [32]. The LCEs in this study correspond to the former case (i.e., parallel), which was confirmed by FTIR spectroscopy [33, 34].

3.2 Electro-Optical Effect

The characteristic two-dimensional deformation of monodomain nematic gels under electric fields originates from the rotation of the director. The electrically driven director rotation is evident from the large change in optical birefringence as shown in Fig. 4b. The appearance of the gel under cross-polarized conditions changes from bright to dark, which corresponds to a change in the director orientation from the x-direction to the z-direction.

Figure 8a shows the effective birefringence (Δn_{eff}: $\Delta n_{\text{eff}} = n_x - n_y$ where n_x and n_y are refractive indices in the x- and y-directions, respectively) in the x–y plane as a function of V_0 [19]. Note that the birefringence data in Fig. 8 was obtained using a cell filled with optically transparent silicone oil in order to observe the optical effect purely originating from the gel, although 5CB was employed as the surrounding fluid in Fig. 4. The gels exhibit a finite Δn_{eff} at $V_0 = 0$ (Δn_{eff}^0) due to the original global uniaxial orientation in the x-direction (i.e., $n_{x0} > n_{y0} = n_{z0}$
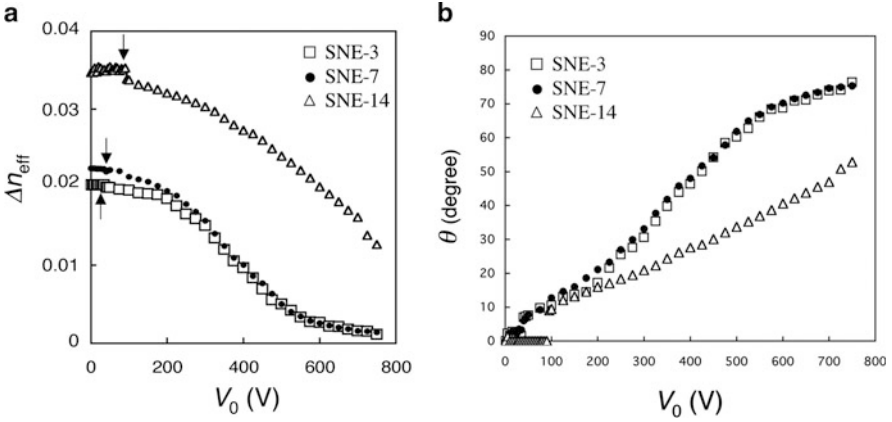
Fig. 8 Electro-optical effect of nematic gels. (**a**) Effective birefringence (Δn_{eff}) as a function of voltage amplitude (V_0). The *arrows* indicate the threshold voltage (V_{0c}) for the onset of deformation, and V_{0c} increases with c_x. (**b**) The V_0 dependence of the rotation angle θ of the director estimated from the birefringence data. The surrounding fluid in the EO cell (Fig. 3) is a silicone oil. From [19]

where n_{i0} is the refractive index in the *i*-direction in the initial state). The birefringence Δn_{eff} decreases with an increase in V_0 above a threshold V_{0c} and it reduces to ca. 5% of the initial value at high V_0 for the specimens with $c_x = 3$ and 7 mol%. This large reduction in Δn_{eff} indicates that sufficiently high V_0 achieves almost full (90°) rotation of the director toward the field direction around the *y*-axis (i.e., $n_x \approx n_{y0} = n_{z0}$). The birefringence is not completely lost, even at high V_0. This is probably because the surface layer firmly anchored in plane does not respond to the field. An increase in c_x suppresses the reduction in Δn_{eff} and increases V_{0c}.

The variations in optical birefringence provide a basis for evaluating the degree of the director rotation. When uniform rotation of the director around the *y*-axis is assumed, the rotation angle (θ) of the director is correlated with Δn_{eff} using the following general relation for systems with uniaxial optical anisotropy ($n_x \geq n_y = n_z$):

$$\sin^2\theta = \frac{n_{y0}{}^2}{n_{x0}{}^2 - n_{y0}{}^2}\left\{\frac{n_{x0}{}^2}{n_x(\theta)^2} - 1\right\} \tag{2}$$

where n_{i0} and $n_i(\theta)$ ($i = x,y$) are the refractive indices along the *i*-axis at $\theta = 0$ and $\theta = \theta$, respectively, and $\theta = 0°$ corresponds to the initial state at $V_0 = 0$ whereas $\theta = 90°$ corresponds to full rotation toward the field direction. If the birefringence is sufficiently small relative to the principal refractive indices, i.e., $n_{y0} \gg \Delta n_{\mathrm{eff}}$ and $n_{y0} \gg \Delta n_{\mathrm{eff}}{}^0$, (2) can be simplified to:

$$\sin^2\theta \approx 1 - \frac{\Delta n_{\mathrm{eff}}(\theta)}{\Delta n_{\mathrm{eff}}{}^0} \tag{3}$$

where $\Delta n_{\mathrm{eff}}^0 = n_{x0} - n_{y0}$. The samples satisfy the condition for this simplification: $\Delta n_{\mathrm{eff}}^0$ is of the order of 10^{-2} whereas the refractive index normal to the long axis ($n_\perp$) for 5CB is ca. 1.5 at 25°C [35]. Figure 8b shows the V_0 dependence of θ obtained using (3) with the data in Fig. 8a. The results demonstrate the rotation process of the director from 0° toward 90°.

3.3 Director Rotation Characterized by Polarized FTIR

The director-rotation behavior under electric fields was also characterized by polarized FTIR [33]. Polarized FTIR has been used to characterize mesogen reorientation and mobility in monodomain LCEs in response to external mechanical fields [25, 36]. The dependence of the absorbance A of a characteristic band on the polarizer angle reflects the average orientation of the bond: A is proportional to $\langle (\boldsymbol{\mu} \cdot \mathbf{E})^2 \rangle$ where vector $\boldsymbol{\mu}$ denotes the molecular transition dipole moment, vector $\mathbf{E}$ denotes the electric field of the IR beam, and the bracket represents averaging over all molecules in the measured region. In usual optical birefringence measurements, the information obtained is only the difference of the contributions in two directions such as $(n_x - n_y)$. Polarized FTIR provides further information about the mesogen reorientation, because this technique gives information about the contribution in each direction separately.

Almost the same observation geometry used in the optical birefringence measurement (Fig. 3) was employed for the polarized FTIR measurements. CaF$_2$ plates with ITO electrodes that are transparent to infrared beams were used. The absorption band of the stretching vibration of the terminal cyano group parallel to the long axes of the mesogens (A-6OCB) and solvent (5CB) at around 2,225 cm^{-1} was used to characterize the director rotation. The absorbances of the incident polarized light parallel and normal to the initial director axis (denoted by A_x' and A_y', respectively) were evaluated from the area of the corresponding peak as a function of V_0. The absorbance of the silicone oil at around the wavelength of interest (2,225 cm^{-1}) was negligible. The absorbances A_x' and A_y' reflect the total contributions from the mesogens of the LCE and the solvent, and they are used to analyze the director-rotation behavior.

Figure 9a shows the V_0 dependencies of the reduced absorbances A_x [$=A_x'/(\lambda_z A_{y0}')$] and A_y [$=A_y'/(\lambda_z A_{y0}')$], where A_x' and A_y' are reduced by λ_z to consider the variation in effective thickness due to deformation, and A_{y0}' is the value of A_y' at $V_0 = 0$. The absorbance A reflects the average orientation of the C≡N bond parallel to the long axis of the mesogens. A finite difference in A_x and A_y at $V_0 = 0$ (denoted A_{x0} and A_{y0}, respectively) reflects the initial uniaxial orientation (original director) in the x-direction. As V_0 increases, the difference in A_x and A_y becomes smaller while A_y remains almost unchanged. Furthermore, A_x becomes nearly equal to A_y at high V_0. When a uniform reorientation of mesogens in the specimen is assumed, A_x and A_y correspond to the long and short axes of the intersection in the x–y plane at

Fig. 9 (**a**) Reduced absorbances (A_x and A_y) as a function of voltage amplitude (V_0) for SNE-7D. (**b**) Absorbance ellipsoid and geometry in polarized FTIR measurements. The coordinate system is the same as in Fig. 3. (**c**) The V_0 dependence of the rotation angle θ of the director estimated from the absorbance data. From [33]
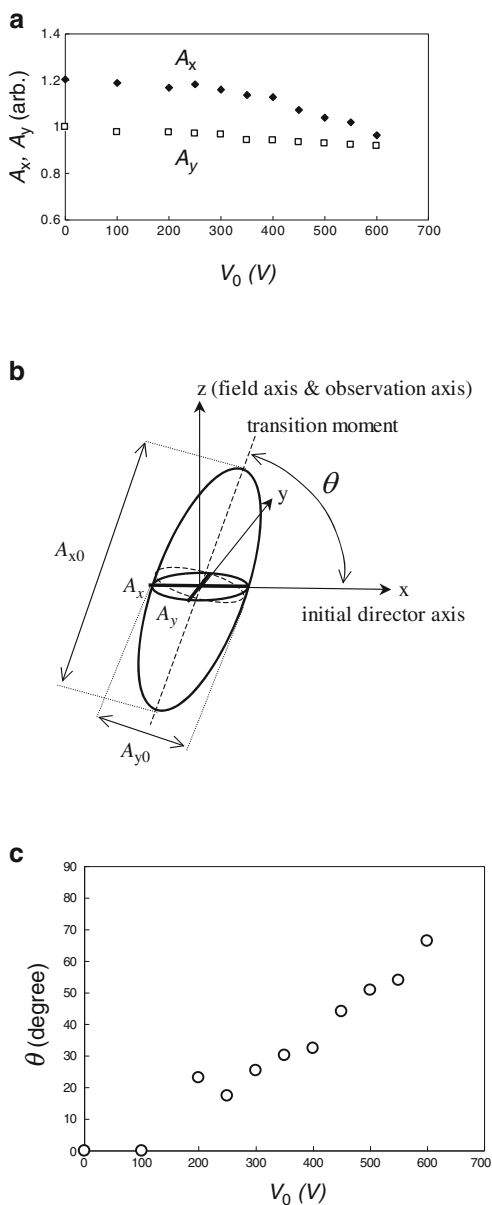
$z = 0$ for the absorption ellipsoid of the director that rotates about the y-axis at an angle of θ (Fig. 9b). The absorbances A_{x0} and A_{y0} at $\theta = 0$ give the long and short axes of the ellipsoid, respectively. The shape of the intersection varies from an ellipse ($A_{x0} > A_{y0}$) to nearly a circle ($A_x \approx A_y$), with almost no change in the short axis ($A_y \approx A_{y0}$). The relation $A_x \approx A_y$ at high V_0 shows a nearly 90° rotation of the

director. In addition, $A_y(V_0) \approx A_{y0}$ indicates that the director rotates around the y-axis with no appreciable change in the orientational order in the plane where the director is confined during the rotation. No macroscopic distortion in the y-direction under electric fields (Fig. 5) results from this type of director rotation.

The absorbance data provide information for estimating the rotation angle θ of the director. In this geometry, $A_x(\theta)$ can be expressed [37] by:

$$A_x(\theta) = a \left[\frac{1-S}{3} + S\cos^2 \theta \right] \tag{4}$$

where a is a constant of proportionality and S is the orientational order parameter of the mesogens. The parameter S is defined by:

$$S = \frac{1}{2} \left[3\langle \cos^2 \phi \rangle - 1 \right] \tag{5}$$

where the bracket denotes the spatial average and ϕ is the angle between the mesogen and the director. In the present case, S is assumed to be independent of θ because the director rotates uniformly around the y-axis. The value of S is obtained from A_{x0} and A_{y0} using the following relation for uniaxial orientation [37]:

$$S = \frac{A_{x0} - A_{y0}}{A_{x0} + 2A_{y0}} \tag{6}$$

From (4) and (6), $\sin^2\theta$ is expressed as a function of A_x:

$$\sin^2 \theta = \frac{A_{x0} - A_x}{A_{x0} - A_{y0}} \tag{7}$$

Figure 9c shows the V_0 dependence of θ evaluated from (7) using the data in Fig. 9a. The same trend as in Fig. 8b based on the birefringence data is observed.

3.4 Correlation Between Director Rotation and Macroscopic Deformation

In addition to the two-dimensional deformation, the correlation between the rotation angle (θ) of the director and the strain (γ_x) gives an important basis for understanding the deformation coupled to director rotation in an unconstrained geometry. Figure 10 shows γ_x and γ_y as a function of $\sin^2\theta$ estimated from the optical birefringence using (3) for the three specimens. In the range examined, γ_x is linearly proportional to $\sin^2\theta$ whereas γ_y is independent of θ. Figure 10 also shows a similar plot using $\sin^2\theta$ evaluated from the polarized FTIR via (7), for SNE-7D.
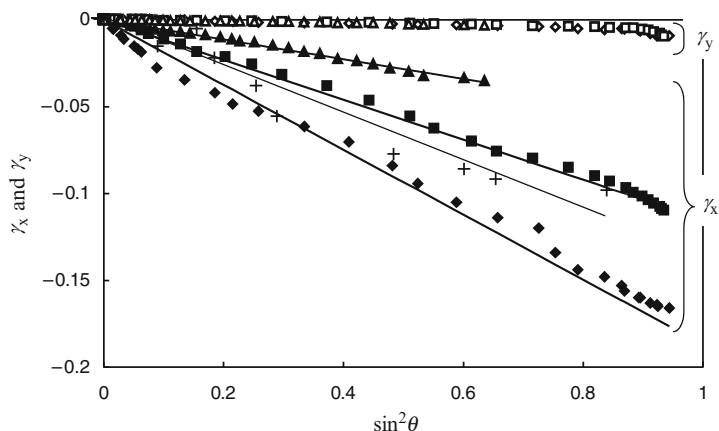
Fig. 10 Strains γ_x (*closed symbols*) and γ_y (*open symbols*) as a function of $\sin^2\theta$ for SNE-3 (*diamonds*), SNE-7 (*squares*), and SNE-14 (*triangles*), where θ is the rotation angle of the director estimated from the birefringence data. The *crosses* represent the data for SNE-7D obtained by polarized FTIR measurements. From [19, 33]
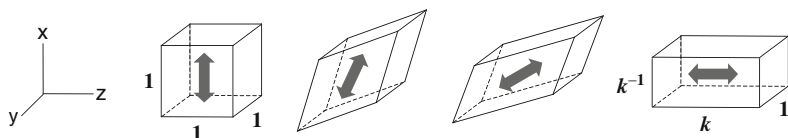

Fig. 11 Deformation of small volume element represented by (8). The *arrow* indicates the director. The rotation angle of director is 0°, 30°, 45°, 60° and 90° from left to right. k elongation, k^{-1} contraction

A linear correlation is observed, and the slope (-0.13) is almost identical with that (-0.12) of the plot using the birefringence data for the similar specimen (SNE-7). This good agreement indicates that the results obtained by the two different methods are consistent. The linear relation $\gamma_x \sim \sin^2\theta$ and the two-dimensional deformation are the two key features of the deformation induced by director rotation for unconstrained nematic elastomers.

Several researchers theoretically considered the deformation mode induced by director rotation in nematic elastomers without external mechanical constraints [1, 38, 39]. The theory is based on the soft elasticity characteristic of ideal nematic elastomers [40]. The expected deformation is a pure shear combined with body rotation, which is illustrated in Fig. 11. When the director rotates by 90°, the cube elongates by k along the realigned director (z) and contracts by k^{-1} along the initial director (x) with no dimensional change along the rotation axis of the director (y). The corresponding deformation gradient tensor is expressed [39] as:

$$\lambda = \begin{pmatrix} 1 - (1 - k^{-1})\sin^2\theta & 0 & (k-1)\sin\theta\cos\theta \\ 0 & 1 & 0 \\ (1 - k^{-1})\sin\theta\cos\theta & 0 & 1 + (k-1)\sin^2\theta \end{pmatrix} \tag{8}$$

where k is a measure of the anisotropy of the dimensions of the constituent polymer chains and is equivalent to the dimensional ratio $l_x(0°)/l_x(90°)$ or $l_z(90°)/l_z(0°)$. The anisotropic Gaussian network model relates k to the orientational order parameter of network backbone (S_B) [1]:

$$k^2 = \frac{1 + 2S_B}{1 - S_B} \tag{9}$$

The dimension l_i ($i = x,y,z$) along the i-axis at $\theta = \theta$ is obtained as:

$$l_x = l_x^0 \left(\lambda_{xx} + \frac{l_z^0}{l_x^0}\lambda_{xz} \right) \approx l_x^0 \lambda_{xx} \tag{10a}$$

$$l_y = l_y^0 \tag{10b}$$

$$l_z = l_z^0 \left(\lambda_{zz} + \frac{l_x^0}{l_z^0}\lambda_{zx} \right) \tag{10c}$$

where λ_{ij} ($i,j=x,y,z$) is the ij component of λ. For sufficiently thin films with $l_z^0/l_x^0 \ll 1$ ($l_z^0/l_x^0 \approx 10^{-2}$ in the present case), the contribution of the shear λ_{xz} to l_x in (10a) is negligible. The expression for γ_i using (1) is given by [19]:

$$\gamma_x = -\left(1 - \frac{1}{k} \right)\sin^2\theta \tag{11a}$$

$$\gamma_y = 0 \tag{11b}$$

$$\gamma_z = (k-1)\sin^2\theta + \frac{l_x^0}{l_z^0}\left(1 - \frac{1}{k} \right)\sin\theta\cos\theta \tag{11c}$$

Most characteristically, the theory predicts γ_x proportional to $\sin^2\theta$ and $\gamma_y = 0$ independent of θ, which accords with the experimental observation.

The value of k estimated from the slope in Fig. 10 for the specimen with $c_x = 7$ mol% is 1.15, which corresponds to $S_B \approx 0.1$. This value of S_B is comparable to the orientational order parameter for the dangling mesogen ($S \approx 0.1$) that was estimated from the absorbance data without an electric field in Fig. 9a. The modest values of S_B and S originate from the swelling effect because S in the dry state is 0.3–0.4.

In a recent paper [41], Corbett and Warner provided a more detailed theoretical explanation for the EOM effects observed by taking into account the deviation from ideal soft elasticity and possible misalignment of the initial director. They also

showed that the deformation is dominated by that driven by director rotation while the contribution of the Maxwell effect to strain is minor, until the director rotation is completed [41].

3.5 Threshold for the Onset of EOM Effect

A finite threshold for the onset of EOM effects is observed in Figs. 5 and 8. In the case of nematic liquids, the determinant of the threshold for the director rotation is voltage, which is a main feature of the Fredericks transition [6, 42]. Does electric field or voltage determine the threshold for LCEs? This issue was first discussed in studies of the EO response of nematic gels in the constrained geometry of $\gamma_z = 0$ [15, 16]. Figure 12 shows Δn_{eff} in the low V_0 region for the two unconstrained samples with the same c_x (14 mol%) but different film thicknesses ($d_g^0 = 23$ and 47 μm) and cell gaps ($d_t = 40$ and 60 μm) [19]. In cells composed of two layers (film and silicone oil) differing in thickness and dielectric constant, the voltage ($V_{c,g}$) and field strength ($E_{c,g}$) acting on the film are given by:

$$V_{c,g} = \frac{\varepsilon_s d_g^0 V_c}{\varepsilon_s d_g^0 + \varepsilon_g \left(d_t - d_g^0\right)} \tag{12a}$$

$$E_{c,g} = \frac{V_{c,g}}{d_g^0} \tag{12b}$$

where ε_g and ε_s are the dielectric constants for the gels along the field axis and silicone oil, respectively. For simplicity, we assume no pre-tilting of nematogens in the initial state, and approximate ε_g by the dielectric constant normal to the long
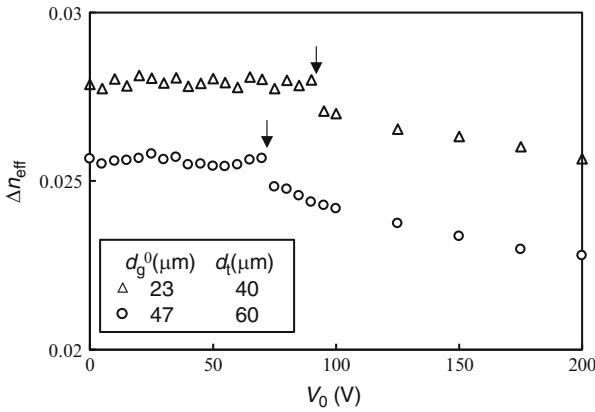

Fig. 12 Effective birefringence (Δn_{eff}) at low-voltage amplitudes for nematic gels with $c_x = 14$ mol% and different values of d_g^0 and d_t. The *arrows* indicate the threshold voltage amplitudes (V_{0c}) for the onset of electro-optical effects. From [19]

axis of 5CB. The calculated values of $V_{c,g}$ and $E_{c,g}$ are $V_{c,g} = 2.1 \times 10^1$ V and $E_{c,g} = 8.2 \times 10^{-1}$ MV/m for $d_g^0 = 23$ μm, and $V_{c,g} = 4.7 \times 10^1$ V and $E_{c,g} = 9.5 \times 10^{-1}$ MV/m for $d_g^0 = 47$ μm. The two samples are largely different in $V_{c,g}$ but similar in $E_{c,g}$. This indicates that the threshold is determined by field rather than voltage, which is similar to the earlier result in the constrained geometry [15, 16]. This results from the different anchoring origins in usual nematic liquids (including uncross-linked nematic polymers) and nematic elastomers (Fig. 1). The anchoring effect in usual nematic liquids stems only from the surface of the electrodes (substrates), whereas the anchoring effect in elastomer solids originates from the bulk elastomer matrix. The initial director is memorized in the whole elastomer matrix at the cross-linking stage. The threshold field $E_{c,g}$ corresponds to the field required to overcome the memory effect of the initial director. A more quantitative discussion of $E_{c,g}$ will be given in Sect. 5.

3.6 Effect of Field Frequency

Figure 13 shows the dependencies of the change in Δn_{eff} and γ_x on frequency (f) of the imposed field for SNE-7 [18]. The two effects have a similar dependence on f. Neither EO nor EM effects are observed at frequencies above 10^5 Hz. When f is too high, it does not induce a dipolar reorientation of the mesogens, as in the case of LMM-LCs. At frequencies less than 10^4 Hz, the EO and EM effects become pronounced. At low frequencies, the deformation and the change in Δn_{eff} increases with f. This may be because of a reduction in the effective voltage amplitude caused by an ionic current of impurities that becomes appreciable at low frequencies.

The dielectric relaxation frequency (f_c) of 5CB at room temperature is in the order of 10^6 Hz [43], whereas f_c of the neat LCE (without solvent) corresponding to SNE-7 (unpublished results from this laboratory) and f_c of an uncross-linked side-chain LC polymer with the similar mesogen [44] are in the order of 10 Hz at 70°C (above the glass transition temperatures of ca. 50°C). The significantly lower values of f_c for the neat LCE and the side-chain LC polymers are due to the constraint effect of the network and polymer backbone on the motion of the dangling
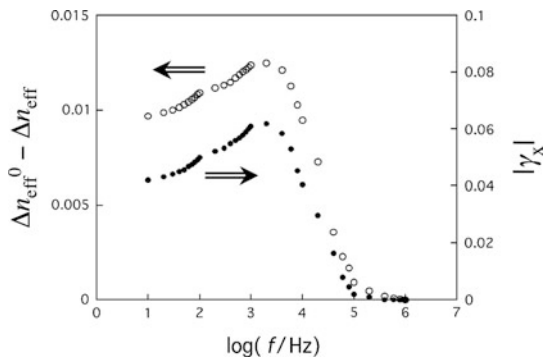

Fig. 13 Effects of field frequency (f) on the strain (γ_x) and the change in optical birefringence (Δn_{eff}) for SNE-7 at $V_0 = 400$ V. From [18]

mesogens. The onset frequency of the EOM effect for SNE-7, which is a mixture of the neat LCE and 5CB, is in the order of 10^4 Hz and lies between the values of f_c of these two components. This result indicates that 5CB inside the gel moves together with the gel matrix, which will also be shown in the dynamics of the EO effects described in Sect. 4.2.

3.7 Effect of Constrained Geometry

The mechanically unconstrained condition is crucial for observing pronounced EOM effects. The imposition of a mechanical constraint considerably suppresses director rotation under electric fields. Figure 14 compares the EO effects of SNE-7 in the constrained and unconstrained states [19]. In the constrained state, the gel is firmly sandwiched by rigid electrodes so that strain in the field direction can be strictly prohibited ($\gamma_z = 0$). In the constrained geometry, the reduction in Δn_{eff} saturates at high fields, and the total drop from the initial value is only 40%. This is considerably smaller than a total drop of ca. 95% in Δn_{eff} in the unconstrained state. In addition, the threshold field strength in the constrained state ($E_{c,g} = 6.3$ MV/m) is an order of magnitude higher than $E_{c,g} = 0.62$ MV/m in the unconstrained state. These results clearly indicate that the geometry prohibiting the deformation strongly suppresses director rotation. This is also a direct consequence of the strong correlation in LCEs between the director and the macroscopic shape.

In the constrained geometry, both deformation and director configuration become considerably nonuniform, and the effect of the Frank elasticity of LCs becomes significant. In contrast, the Frank elasticity has essentially no role in the unconstrained case where the director rotates uniformly. Some theoretical studies [16, 45, 46] suggest that several characteristic patterns of director configuration and macroscopic distortion appear, depending on the nematicity, film thickness, and field strength. The corresponding experimental studies [16] are quite limited because of
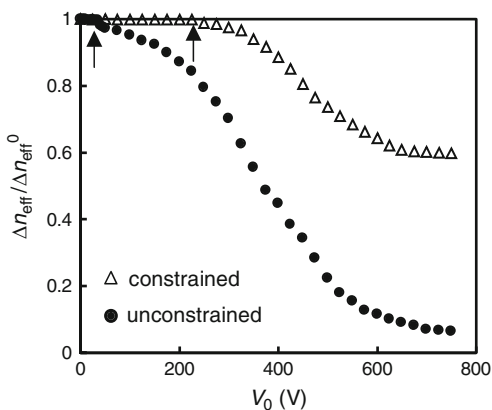

Fig. 14 Effect of mechanical constraints on electro-optical effects for SNE-7. The *arrows* indicate the threshold voltage amplitudes (V_{0c}) for the onset of electro-optical effects. From [19]

the difficulty of direct observation of the deformation and director rotation in the x–z plane. A rich variety of expected patterns of director configuration and deformation in a constrained geometry are an interesting characteristic of LCEs that possess the two types of elasticity, i.e., rubber elasticity and Frank elasticity.

4 Dynamic Aspects

4.1 Rise and Decay Times

In this section, we describe the dynamic features of EOM effects. In particular, we focus on the response times to field-on and field-off; these are the rise and decay times, respectively. In the case of the EO effects of nematic liquids, the rise and decay times exhibit the characteristic dependencies on voltage, and these characteristic times reflect the elastic, viscous, and dielectric properties of the materials. They have fully characterized the dynamics of the electric-field responses of LMM-LCs in experiments and established the theoretical background [6]. The dynamic features of the EOM effects in nematic gels are expected to differ from those of the EO effects in LMM-LCs, because the gels possess rubber elasticity and also have a different origin of the memory of the initial director. In addition, the dynamic properties give important information about the applicability of EOM effects in practical applications.

Figure 15 shows examples of the time courses of EO and EM effects in response to the imposition and removal of electric fields. These effects require a finite time to reach steady states after the field imposition, and to recover the initial states after the field removal. The rise and decay times were defined to be the times required for 70% of the total change. Figure 16 displays the optical and mechanical rise times (designated as $\tau_{\mathrm{on}}{}^{\Delta n}$ and $\tau_{\mathrm{on}}{}^{\gamma}$, respectively) as a function of the field strength acting on the specimen (E_{g}). The optical rise times are of the order of milliseconds and almost proportional to E_{g}^{-2}, which is similar to that for pure LMM-LCs. The E_{g} dependence of $\tau_{\mathrm{on}}{}^{\gamma}$ is also approximated by $\tau_{\mathrm{on}}{}^{\gamma} \sim E_{\mathrm{g}}^{-2}$, but $\tau_{\mathrm{on}}{}^{\gamma}$ is about an order of magnitude larger than $\tau_{\mathrm{on}}{}^{\Delta n}$. An increase in the cross-linker concentration results in an increase in $\tau_{\mathrm{on}}{}^{\Delta n}$ and a slight increase in $\tau_{\mathrm{on}}{}^{\gamma}$.

Figure 17 shows the optical and mechanical decay times ($\tau_{\mathrm{off}}{}^{\Delta n}$ and $\tau_{\mathrm{off}}{}^{\gamma}$, respectively) as a function of E_{g}. Both $\tau_{\mathrm{off}}{}^{\Delta n}$ and $\tau_{\mathrm{off}}{}^{\gamma}$ are substantially independent of E_{g}, similarly to $\tau_{\mathrm{off}}{}^{\Delta n}$ for LMM-LCs. As in the case of the rise times for the mechanical and optical responses, $\tau_{\mathrm{off}}{}^{\gamma}$ is about ten times larger than $\tau_{\mathrm{off}}{}^{\Delta n}$.

The trigger of the EM effects in nematic elastomers is the rotation or recovery of the director, each of which is observed as an EO effect. The deformation follows the motion of the director. The finite retardation of EM effects is probably due to viscoelastic effects, or a time lag between the orientation of dangling mesogens and the induced deformation of network backbone. The dynamics of EOM effects for main-chain type nematic gels will give important information about this issue.
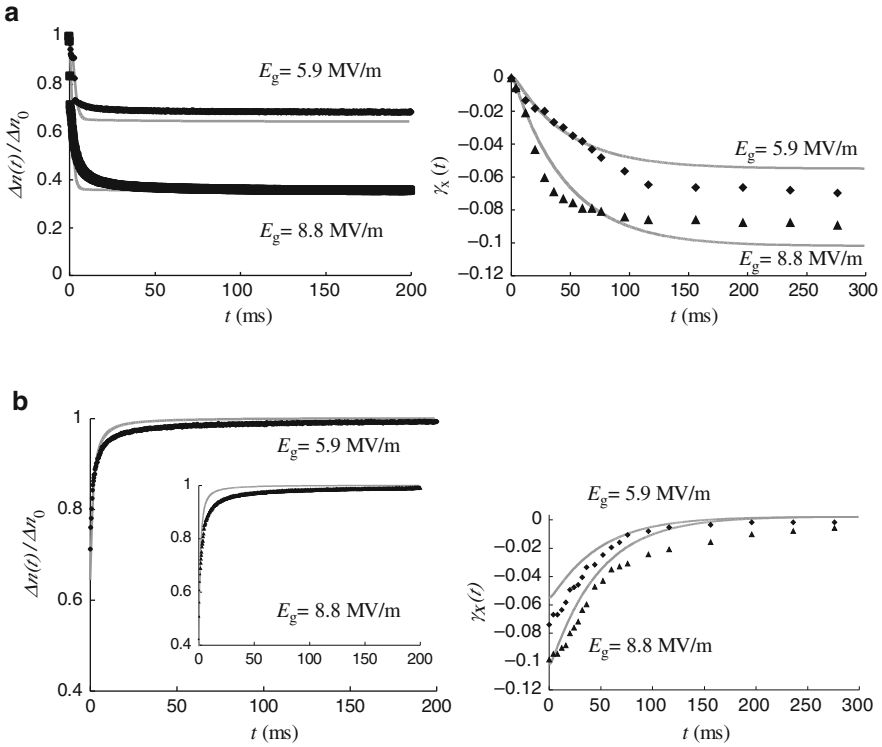
a

b

Fig. 15 Time courses of optical birefringence (Δn) and strain (γ_x) after (**a**) applying and (**b**) removing fields of 5.9 and 8.8 MV/m for SNE-7D. The *gray solid lines* indicate the numerical results obtained from the model. From [31]
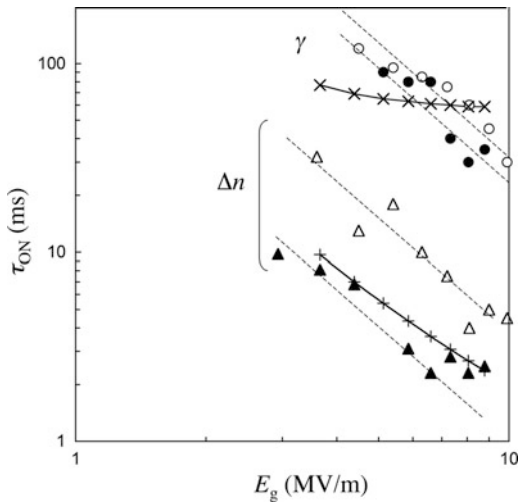

Fig. 16 Optical (Δn) and mechanical (γ) rise times (τ_{ON}) as a function of field strength E_g for SNE-7D (*closed symbols*) and SNE-10D (*open symbols*). The slope of the *dashed lines* is 2. The *crosses* indicate the theoretical results fitted to the data for SNE-7D. From [31]

Fig. 17 Optical (Δn) and mechanical (γ) decay times (τ_{off}) as a function of field strength E_{g} for SNE-7D (*closed symbols*) and SNE-10D (*open symbols*). The *crosses* indicate the theoretical results fitted to the data of SNE-7D. From [31]
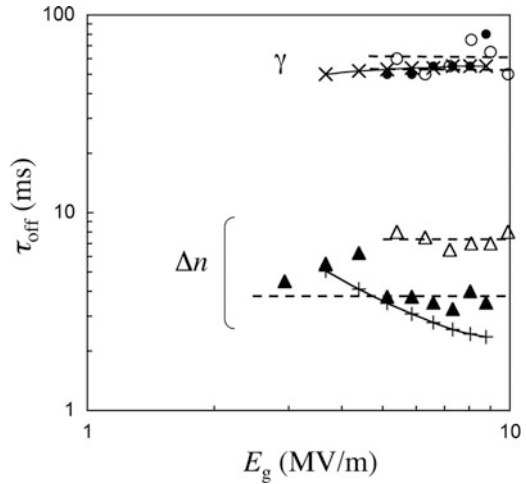
4.2 Comparison of Dynamics for Swollen Nematic Elastomers and Nematic Liquids

The optical decay times directly reflect the recovery force of the director inherent in the materials, as is physically evident from the independence of field strength. In the case of nematic liquids, the recovery force originates from Frank elasticity. As a result, $\tau_{\text{off}}^{\Delta n}$ strongly depends on cell thickness (d_{cell}) and becomes smaller with a decrease in d_{cell} as $\tau_{\text{off}}^{\Delta n} \sim d_{\text{cell}}^{-2}$. It is interesting to compare $\tau_{\text{off}}^{\Delta n}$ for SNE-7D and the pure LMM-LC (5CB; swelling solvent) confined in a cell with a gap of 25 μm that is comparable to the gel thickness: $\tau_{\text{off}}^{\Delta n}$ for the nematic gel (ca. 3 ms) is about three orders of magnitude smaller than that (ca. 2 s) for the pure 5CB, despite the high content of 5CB (78 vol%). The recovery force of the director in nematic gels originates from the memory effect of the initial director that is imprinted in the cross-linking stage. Since this memory is a bulk matrix effect, the decay time is independent of gel thickness, in contrast to that for nematic liquids strongly depending on d_{cell}. The recovery force in nematic gels is considerably stronger than that (Frank elasticity) in nematic liquids. The results also indicate that the solvent inside the gels moves together with the gel matrix.

5 Simple Model Capturing Main Features

A minimal model for interpreting the main features of the static and dynamic aspects of EOM effects [31] is introduced in this section. To reduce complexity, this model does not explicitly consider the anisotropic effect on elastic and viscous properties. More realistic expressions considering the anisotropy [47–50] are available, but the limited experimental data makes it difficult to unambiguously determine a larger set of material parameters.

The free energy of nematic gels under electric fields may be written as the sum of the Frank energy (F_F), the electrostatic energy (F_{el}), and the gel elasticity energy (F_g):

$$F = F_F + F_{el} + F_g \tag{13}$$

It should be noted that $F_F \approx 0$ in the present case where the director rotates uniformly around the y-axis, i.e., the director is always confined to the x–z plane.

The electrostatic energy is:

$$F_{el} = -\frac{\varepsilon_0}{2} \int_A (\varepsilon_a (\nabla\varphi(x) \cdot \mathbf{n}(x))^2 + \varepsilon_\perp |\nabla\varphi(x)|^2) dx - \frac{\varepsilon_0}{2} \int_B (\varepsilon_s |\nabla\varphi(x)|^2) dx \tag{14}$$

where φ is the electric potential, $\mathbf{n} = (\cos\theta, 0, \sin\theta)$ is the nematic director, and A and B are the spaces occupied by gel and silicone oil, respectively. The dielectric constant ε_s is for silicone oil, whereas $\varepsilon_\parallel$ and $\varepsilon_\perp$ are those parallel and normal to $\mathbf{n}$ for the gel, respectively, and $\varepsilon_a = \varepsilon_\parallel - \varepsilon_\perp$.

The elastic energy of the gel is:

$$F_g = \int \left[\frac{G}{2} |e_u(x) - e_0(\mathbf{n}(x))|^2 + f_{an}(\mathbf{n}(x)) \right] dx \tag{15}$$

where G is the shear modulus and e_u is the linear strain with components $(e_u)_{ij} = (\partial u_i/\partial x_j + \partial u_j/\partial x_i)/2$. The quantity $u_i(x)$ is the ith component of the displacement at point x of the gel with respect to its reference configuration (chosen as the configuration the specimen would take in a high-temperature isotropic state), and x_j is the jth coordinate of x. The strain $e_0(\mathbf{n})$ corresponds to that in the stress-free state associated with $\mathbf{n}$, which we assume to be a uniaxial stretching along n. This is expressed by the following matrix as a function of the angle θ:

$$[e_0(\mathbf{n})] = \begin{bmatrix} \frac{3}{2}g(\cos^2\theta - \frac{1}{3}) & 0 & \frac{3}{2}g\sin\theta\cos\theta \\ 0 & -\frac{g}{2} & 0 \\ \frac{3}{2}g\sin\theta\cos\theta & 0 & \frac{3}{2}g(\sin^2\theta - \frac{1}{3}) \end{bmatrix} = [e_0(\theta)] \tag{16}$$

where g is a measure of the chain anisotropy in the gel and related to k as $g = 2(k-1)/(k+2)$. The dimensional variation in the x direction driven by the rotation (θ) of the director in the x–z plane is given by $(e_u)_{11} = [e_0(\theta)]_{11}$. The corresponding strain γ_x is given by:

$$\gamma_x(\theta) = \frac{l_x(\theta) - l_x^0}{l_x^0} = \frac{[e_0(\theta)]_{11} - [e_0(0)]_{11}}{1 + [e_0(0)]_{11}} = -\frac{3g}{2(1+g)}\sin^2\theta \tag{17}$$

This relation is substantially equivalent to (11a) since the parameter k is given by $k = l_x(0)/l_x(90°)$.

In (15), f_{an} is the anisotropic energy density for the memory effect of the director, driving the director $\mathbf{n}$ towards the initial director $\mathbf{n_0} = (1,0,0)$ at cross-linking.

The phenomenological expression of f_{an} may be given by the elastic energy of a nonlinear spring with the two independent constants k_1 and k_2:

$$f_{an}(\mathbf{n}) = \frac{k_1}{2}\sin^2\theta + \frac{k_2}{4}\sin^4\theta \tag{18}$$

A similar expression is found in [50] and in (8.30) of [1].

The dynamics of a nematic gel are assumed to be governed by the viscoelasticity of the gel, the rotational viscoelasticity of the director, and electrostatics. The governing equations for the dynamics are derived from the balance between the rates of free-energy release and viscous dissipation. In the present case, strain rates and stresses are spatially uniform because of the unconstrained geometry. Therefore, the governing equations for the dynamics of the strain and the director are obtained from the free energy as [31]:

$$\eta_g \frac{d}{dt}e_u = -G[e_u - e_0(n)] \tag{19}$$

and

$$\eta_n \frac{d}{dt}\theta = T_G + T_{an} + T_\varphi \tag{20}$$

where η_g and η_n are the frictional coefficients of the deformation and the director motion, respectively. In (20), the elastic torque T_G, the restoring torque T_{an}, and the electrostatic torque T_φ are given by:

$$T_G = 3Gg\{(e_u)_{13}(\cos^2\theta - \sin^2\theta) + [(e_u)_{33} - (e_u)_{11}]\sin\theta\cos\theta\} \tag{21a}$$

$$T_{an} = -(k_1 + k_2\sin^2\theta)\sin\theta\cos\theta \tag{21b}$$

$$T_\varphi = \varepsilon_0\varepsilon_a\left(\frac{V_0}{d(\theta)}\right)^2\sin\theta\cos\theta \tag{21c}$$

Note that only the 11, the 33, and the 13 strain components are nontrivial because the director rotates in the x–z plane.

In the steady state ($de_u/dt = 0$), the relation $e_u \equiv e_0(n)$ is obtained from (19). Equation (21a) with this relation leads to $T_G = 0$ in the steady state. Therefore, the torque balance equation for the director in the steady state is given from (20) as:

$$0 = T_{an} + T_\varphi \tag{22}$$

The equilibrium values of θ and γ (θ^s and γ^s, respectively) at each V_0 are calculated from (17) and (22). Figure 18 shows a comparison of the steady-state
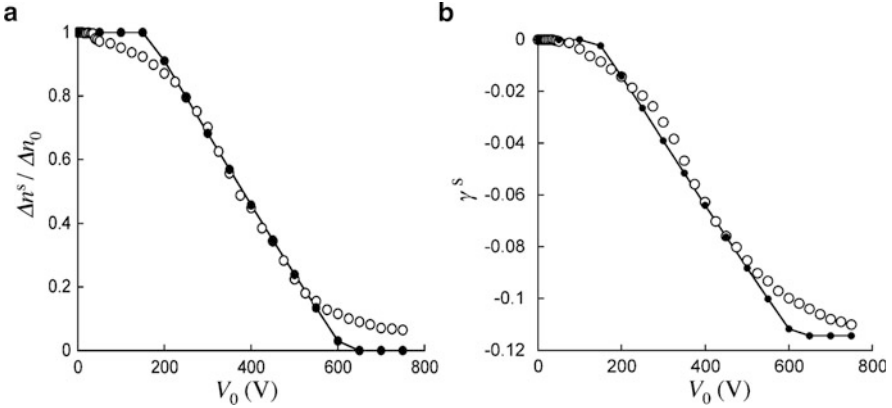
Fig. 18 Numerical (*closed symbols*) versus experimental (*open symbols*) results for (**a**) optical birefringence (Δn) and (**b**) strain in the steady state (γ^S) as a function of voltage amplitude (V_0). From [31]

data for SNE-7 with the theoretical results using the fitted parameter values of $g = 0.0825$, $k_1 = 650$ J/m^3 and $k_2 = 4{,}100$ J/m^3. The theoretical value of reduced birefringence $\Delta n^s/\Delta n_0$ in the figure is given by $\cos^2\theta^s$ [see (3)]. The theoretical results describe the main features in the experimental data such as the presence of the threshold for the onset of director rotation and the maximum value of strain at high voltages. The theoretical strain reaches a maximum at $\theta = 90°$, where the birefringence becomes zero, and $|\gamma^s|_{max}$ is given by $3g/[2(1 + g)]$ ($\equiv 1 - k^{-1}$). The theoretical expression for the threshold field strength $E_{g,c}$ for the gel is obtained from (22) as:

$$E_{g,c} = \sqrt{\frac{k_1}{\varepsilon_0 \varepsilon_a}} \tag{23}$$

This equation gives a physical explanation for the threshold for director rotation. The threshold is determined by field strength rather than voltage, and the director starts to rotate when the dielectric force overcomes the strength of the memory of the initial director at cross-linking.

The time courses of Δn_{eff} and γ in response to field-on and field-off are computed from (19) and (20). The gray solid lines in Fig. 15 indicate the numerical results for $E_g = 5.9$ and 8.8 MV/m. It should be noted that when selecting the material parameter values, we first tune the parameters g, k_1, and k_2 to fit the steady-state data (see Fig. 7 in [31] for specimen SNE-7D in Fig. 15). Then, using these values ($g = 0.12$, $k_1 = 300$ J/m^3 and $k_2 = 6{,}000$ J/m^3), we tune the parameters η_g, η_n, and G to fit the dynamic data: $\eta_g = 50$ Js/m^3, $\eta_n = 12$ Js/m^3 and $G = 2{,}000$ J/m^3. The theoretical values of the rise times for the optical and mechanical responses are compared with the experimental data in Fig. 16. The model successfully describes the $\tau_{on}^{\Delta n} \sim E_g^{-2}$ behavior in the experiments. In contrast, the model exhibits a much weaker E_g dependence of τ_{on}^{γ} than the experiments suggest. In Fig. 17, the

theoretical values of the optical and mechanical decay times are compared with the experimental values. The theory captures well the lack of E_g dependence of τ_{off}^{γ} observed in the experiments. However, the theoretical $\tau_{off}^{\Delta n}$ values are slightly E_g-dependent in contrast to the experimental values that are substantially independent of E_g. These discrepancies originate from the fact that the real response times for director and deformation are not as widely separated as assumed in the model.

It is worth comparing the viscous coefficients for swollen nematic elastomers obtained here with those in neat elastomers as estimated from dynamic light scattering [51]. The relaxation times $\tau_{off}^{\Delta n}$ for the director in Fig. 17 are not very different from those in Fig. 5 in [51] in view of the finite difference in elastic modulus between the neat and swollen states. The swollen nematic elastomers are considerably softer than the neat ones: k_1 is two orders of magnitude smaller than D_1 in [51]. Correspondingly, the viscous coefficient η_n for the director in the gels, estimated from $\tau_{off}^{\Delta n} \approx \eta_n/k_1$, is significantly smaller than the η_{loss} in neat elastomers, evaluated from $\tau \approx \eta_{loss}/D_1$.

6 Conclusion and Outlook

Nematic elastomers swollen by LMM-LCs (nematic gels) exhibit pronounced EM effects combined with EO effects. This EOM effect is a direct consequence of the macroscopic deformation driven by electrically induced director rotation. Swelling by LMM-LCs considerably reduces the field strength for actuation, because of a significant softening of the nematic elastomers without loss of the liquid crystallinity. The electrical strain in nematic gels primarily originates from the strain caused by director realignment. The stretching direction is governed by the direction of the molecular long axis of mesogens under electric fields: the dielectrically positive and negative nematic gels are elongated in the directions parallel and normal to the field axis, respectively. External mechanical constraints to prohibit the strain in one direction considerably suppress the director reorientation and resultant deformation under electric fields.

The director rotation is considerably facilitated under unconstrained conditions where the gel floats in fluid between rigid electrodes whose gap is larger than the gel thickness. The monodomain nematic gels under electric fields exhibit a two-dimensional deformation where the dimension along the initial director decreases, and the dimension along the field axis increases, without an appreciable dimensional change along the rotation axis of the director. The director of unconstrained monodomain nematic gels rotates purely around the axis normal to both the field and initial director axes, leading to the two-dimensional distortion. Characteristically, the strain is almost linearly proportional to $\sin^2\theta$ (where θ is the rotation angle of the director). This behavior is in good agreement with the predictions of soft elasticity theory for thin nematic elastomer films in which the shear contribution is negligible.

The rise and decay times of the EOM effects are similar in their dependencies on field strength to those of the EO effect of LMM-LCs, although the mechanical

response times are about an order of magnitude larger than the optical times. Importantly, the recovery rate of the director (estimated from the optical decay time) in nematic gels is about three orders of magnitude higher than that in LMM-LCs confined in the cell with the same gap as the gel thickness. This indicates that the memory effect of the initial director, which is imprinted at cross-linking, is much stronger than the Frank elasticity. The memory effect of the initial director in nematic gels is a bulk matrix effect. This is also recognized by the fact that the threshold for the onset of EOM effects is determined by the field strength, in contrast to the Fredericks transition of LMM-LCs whose threshold is determined by voltage.

So far, EOM effects have been reported for only a limited number of nematic gels. There is great potential for enhancing the performance of the electric-field response. The molecular characteristics of nematic elastomers and solvents have not yet been optimized for high performance. Possible options might include: (1) employment of main-chain-type nematic elastomers; (2) optimization of the cross-linker geometry; and (3) an increase in the dielectric anisotropy of mesogens. The first and second options are aimed at increasing the electrical strain, i.e., enhancing the coupling between mesogen orientation and macroscopic deformation. Many investigations of thermally induced deformation have indicated that these options are effective for this purpose. The third option contributes to reducing the actuation voltage [see (23)] and to shortening the field-on response time. This is based on an analogy with the effect of dielectric anisotropy on EO effects in LMM-LCs.

The EM effects of nematic elastomers have great potential for practical applications such as soft actuators. For practical purposes, actuation must be fast and low-voltage with a large strain (generating a large stress). Establishing the fundamentals of the molecular design of nematic elastomers with high EM performance will also meet these industrial demands.

References

1. Warner M, Terentjev EM (2007) Liquid crystals elastomers (revised edition). Clarendon, London
2. Xie P, Zhang RJ (2005) J Mater Chem 15:2529
3. Brand HR, Pleiner H, Martinoty P (2006) Soft Matter 2:182
4. Urayama K (2007) Macromolecules 40:2277

5. Kramer D, Brömmel F, Finkelmann H (2011) In: De Jeu WH (ed) Liquid crystal elastomers: materials and applications. Adv Polym Sci. Springer, Heidelberg, Berlin, doi: 10.1007/12_2012_168
6. Oswald P, Pieranski P (2005) Nematic and cholesteric liquid crystals. CRC, Boca Raton
7. Lehmann W, Skupin H, Tolksdorf C, Gebhard E, Zentel R, Kruger P, Lösche M, Kremer F (2001) Nature 410:447
8. Spillmann CM, Ratna BR, Naciri J (2007) J Appl Phys Lett 90
9. Zentel R (1986) Liq Cryst 1:589
10. Barnes NR, Davis FJ, Mitchell GR (1989) Mol Cryst Liq Cryst 168:13
11. Kishi R, Suzuki Y, Ichijo H, Hirasa O (1994) Chem Lett:2257
12. Huang C, Zhang QM, Jakli A (2003) Adv Funct Mater 13:525
13. Urayama K, Kondo H, Arai YO, Takigawa T (2005) Phys Rev E 71:051713
14. Yusuf Y, Huh JH, Cladis PE, Brand HR, Finkelmann H, Kai S (2005) Phys Rev E 71:061702
15. Chang CC, Chien LC, Meyer RB (1997) Phys Rev E 56:595
16. Terentjev EM, Warner M, Meyer RB, Yamamoto J (1999) Phys Rev E 60:1872
17. Terentjev EM, Warner M, Bladon P (1994) J Phys (Paris) II 4:667
18. Urayama K, Honda S, Takigawa T (2005) Macromolecules 38:3574
19. Urayama K, Honda S, Takigawa T (2006) Macromolecules 39:1943
20. Zubarev ER, Talroze RV, Yuranova TI, Plate NA, Finkelmann H (1998) Macromolecules 31:3566
21. Mitchell GR, Davis FJ, Guo W (1993) Phys Rev Lett 71:2947
22. Roberts PMS, Mitchell GR, Davis FJ (1997) J Phys (Paris) II 7:1337
23. Kundler I, Finkelmann H (1995) Macromol Rapid Commun 16:679
24. Tammer M, Li JJ, Komp A, Finkelmann H, Kremer F (2005) Macromol Chem Phys 206:709
25. Li J, Tammer M, Kremer F, Komp A, Finkelmann H (2005) Eur Phys J E 17:423
26. Verwey GC, Warner M, Terentjev EM (1996) J Phys (Paris) II 6:1273
27. Conti S, DeSimone A, Dolzmann G (2002) J Mech Phys Solids 50:1431
28. Fried E, Sellers S (2006) J Appl Phys 100:043521
29. Urayama K, Arai YO, Takigawa T (2005) Macromolecules 38:3469
30. Urayama K, Arai YO, Takigawa T (2005) Macromolecules 38:5721
31. Fukunaga A, Urayama K, Takigawa T, DeSimone A, Teresi L (2008) Macromolecules 41:9389
32. Finkelmann H, Kock HJ, Gleim W, Rehage G (1984) Makromol Chem Rapid Commun 5:287
33. Fukunaga A, Urayama K, Koelsch P, Takigawa T (2009) Phys Rev E 79:051702
34. Urayama K, Mashita R, Kobayashi I, Takigawa T (2007) Macromolecules 40:7665
35. Simon R, Nicholas DM (1985) J Phys D Appl Phys 18:1423
36. Aksenov V, Stannarius R, Tammer M, Kolsch P, Kremer F, Rossle M, Zentel R (2007) Liq Cryst 34:87
37. Zbinden R (1964) Infrared spectroscopy of high polymers. Academic, New York
38. Olmsted PD (1994) J Phys (Paris) II 4:2215
39. Verwey GC, Warner M (1995) Macromolecules 28:4303
40. Warner M, Bladon P, Terentjev EM (1994) J Phys (Paris) II 4:93
41. Corbett D, Warner M (2009) Soft Matter 5:1433
42. de Gennes PG, Prost J (1993) The physics of liquid crystals, 2nd edn. Oxford University Press, New York
43. Kreul H-G, Urban S, Wurflinger A (1992) Phys Rev A 45:8624
44. Garcia-Bernabe A, Diaz-Calleja R (2001) Polym Int 50:165
45. Skacej G, Zannoni C (2006) Eur Phys J E 20:289
46. Muller O, Brand HR (2005) Eur Phys J E 17:53
47. Terentjev EM, Warner M (2001) Eur Phys J E 4:343
48. Fradkin LJ, Kamotski IV, Terentjev EM, Zakharov DD (2003) Proc R Soc Lond Ser A Math Phys Eng Sci 459:2627
49. Martinoty P, Stein P, Finkelmann H, Pleiner H, Brand HR (2004) Eur Phys J E 14:311
50. Teixeira PIC, Warner M (1999) Phys Rev E 60:603
51. Schonstein M, Stille W, Strobl G (2001) Eur Phys J E 5:511